ADVANCED MATERIALS INTERFACES
Open Access
www.advmatinterfaces.de

The Fabrication of Fluorine-Free Stretchable Superhydrophobic Films Using Inverse Vulcanization Sulfur Polymer

Vinicius Diniz, Nicola M. Pugno, Susanne Rath, and Colin R. Crick**

Stretchable superhydrophobic materials have gained attention in recent years though challenges remain for widespread use, including the need for rapid, energy-efficient, high-throughput, and fluorine-free fabrication methods. In this study, a stretchable superhydrophobic material is developed by coating parafilm with inverse vulcanization sulfur polymers. Silica (SiO_2) nanoparticles are incorporated to create a Cassie–Baxter wetting state, achieving superhydrophobicity. The sulfur polymers are synthesized using perillyl alcohol (PER) at varying sulfur-to-PER ratios. The optimal coating formulation is determined to be 70 mg mL^{-1} of polymer, 50 mg mL^{-1} of SiO_2 nanoparticles, and a sulfur-to-PER ratio of 1:1 (50% sulfur and 50% PER). The films maintained functionality when stretched due to controlled fragmentation that preserved the Cassie–Baxter wetting state. Mathematical modeling revealed a scaling relation between fragment area and thickness, showing that thicker layers produced larger fragments, impairing superhydrophobicity. This study also showcase the successful use of more sustainable bio-based solvents (2-methyltetrahydrofuran), where previous reports of similar processes have used chloroform. The fabricated films also demonstrated improved ultraviolet (UV-C) stability (150 min) compared to other sulfur polymer coatings reported in the literature. This coating of flexible substrates presents a simple and environmentally friendly method for producing stretchable superhydrophobic films.

1. Introduction

Inspired by nature's water-repellent surfaces, such as lotus leaves and moth eyes, superhydrophobic surfaces exhibit exceptional water repellency.[1,2] On these surfaces, water droplets form nearly perfect spheres due to high receding contact angles above 150°.[3] This superhydrophobicity is achieved through a combination of micro/nano/hierarchical structures and low-surface-energy materials (hydrophobic chemistry), creating a Cassie–Baxter state where an air layer forms between the droplet and the solid substrate.[4–6] This air layer is crucial for maintaining the droplet's spherical shape and preventing the liquid from wetting the surface protrusions, ensuring mechanical durability and stability.[7,8]

Superhydrophobic surfaces, with their low liquid adhesion and minimal contact area between water droplets and the solid substrate, have significant potential in various applications, including antifouling,[9,10] oil–water separation,[11,12] self-cleaning,[4,13,14] and anti-corrosion.[9,15] Although numerous strategies have been explored to achieve superhydrophobic surfaces, practical applications are often hindered by expensive manufacturing processes and the fragility of rigid inorganic structures.[16,17]

In contrast to these rigid materials, soft materials can maintain their properties after mechanical deformation, such as bending, pressing, and stretching. This flexibility offers a significant advantage in creating durable superhydrophobic surfaces that can withstand mechanical stress, leading to more robust and long-lasting coatings. Stretchable

V. Diniz, N. M. Pugno, C. R. Crick
School of Engineering and Materials Sciences
Queen Mary University of London
London E1 4NS, UK
E-mail: v.diniz@qmul.ac.uk; c.crick@qmul.ac.uk

The ORCID identification number(s) for the author(s) of this article can be found under https://doi.org/10.1002/admi.202400896

DOI: 10.1002/admi.202400896

V. Diniz, S. Rath
Institute of Chemistry
University of Campinas
Campinas 13083–970, Brazil

N. M. Pugno
Laboratory for Bioinspired, Bionic
Nano, Meta Materials and Mechanics
Department of Civil
Environmental and Mechanical Engineering
University of Trento
via Mesiano 77, Trento 38123, Italy

superhydrophobic surfaces have been proposed in recent years for various applications, such as strain sensors for real-time monitoring, efficient oil-water separation, anti-icing to prevent ice accumulation, droplet manipulation in microfluidics, and corrosion prevention by protecting materials from moisture.[17–22] However, significant limitations and challenges persist that must be resolved for effective real-world applications.[17] Key challenges include the need for streamlined, rapid, energy-efficient, and high-throughput fabrication techniques to simplify the complexities of conventional methods, as well as the development of fluorine-free materials due to the environmental concerns associated with fluorine-containing compounds.[17] In addition, the direct dependence of surface wettability on morphology means that as materials are stretched (through flexing or fragmentation), the surface wetting may vary significantly. Therefore, flexible superhydrophobic materials must have a predictable and reproducible flexing/fragmentation behavior in order to be most widely applicable.

Inverse vulcanization sulfur polymers have emerged as a promising solution for superhydrophobic applications, offering a more sustainable alternative to conventional hydrophobic materials.[4,13,23–25] These polymers are synthesized through a process that utilizes elemental sulfur, a byproduct of the petrochemical industry, combined with various organic crosslinkers.[26] The result is a polymer with high sulfur content, which can be tailored to provide excellent hydrophobic properties but also contributes to the material's environmental friendliness.[4,13,23,27] The inverse vulcanization process is relatively simple and energy-efficient, making it an attractive option for large-scale production.[25] These sulfur polymers can form the basis of superhydrophobic coatings by creating a hydrophobic chemistry, which is essential for achieving the desired water-repellent properties. Additionally, the inherent chemical resistance and durability of sulfur polymers make them well-suited for applications requiring long-term stability and robustness.[4] By replacing fluorine-containing compounds, which pose environmental concerns, with these high-sulfur-content polymers, researchers can develop more sustainable and effective superhydrophobic surfaces.

In this research, we report the fabrication of fluorine-free stretchable superhydrophobic films by the spray-coating of silica (SiO_2)/sulfur polymer layers onto parafilm. Parafilm consists of a blend of waxes and polyolefins that are inherently hydrophobic. Moreover, it can stretch to over 200% of its original length, making it an excellent substrate for stretchable superhydrophobic films. SiO_2 nanoparticles facilitate the creation of the hierarchical roughness structure essential for superhydrophobicity. At the same time, sulfur polymers act as binders, enhancing adhesion between the coating formulation and parafilm and improving the hydrophobic chemistry of the formulation. Additionally, the study investigated how varying the coating thickness impacts the fragmentation of the top layer coating (i.e., sulfur polymer), which in turn affects the wettability properties after stretching. This analysis provided insights into the relationship between coating thickness and the resulting superhydrophobic performance. The results indicated that the optimal loading of SiO_2 nanoparticles and polymer concentration produced stretchable films (>200%) that are able to maintain their superhydrophobicity (WCA > 150°). However, for thicker coatings (>42 µm), it was observed a significant increase in fragment size after stretching, which, consequently, impaired the superhydrophobic properties. Furthermore, this research demonstrated that a bio-based solvent, 2-methyltetrahydrofuran, could replace the commonly used chloroform for spraying sulfur polymer without affecting the wettability and ultraviolet (UV-C) stability of the films. This study highlights the potential for a new class of more sustainable and easily fabricated stretchable superhydrophobic polymer-nanoparticle composite films. These findings offer promising alternatives to conventional, time-consuming, and environmentally harmful materials and provide valuable insights into how the fragmentation of thin films affects their wettability.

2. Experimental Section

2.1. Chemical and Reagents

Elemental sulfur (S_8, sublimed powder, reagent grade, ≥99.5%) was purchased from Honeywell Research Chemicals (UK). Hexamethyldisilazane (≥99.0%), (S)-(−)-perillyl alcohol (≥95%), and SiO_2 (Ø = 10–20 nm) were purchased from Merck Ltd. (UK). 2-Methyltetrahydrofuran (99%), acetone (>95%), chloroform (99.8%), dimethylformamide (99.8%), hexane (≥95%), isopropanol (99.8%), tetrahydrofuran (99+ %), toluene (99.8+ %), ethanol (analytical reagent grade), and Parafilm M (roll dimensions; 50 mm × 75 m) were purchased from Fischer Scientific Ltd. (UK). Deuterated chloroform (99.8%) was purchased from Cambridge Isotopes Laboratories Ltd. (UK).

2.2. Synthesis of Poly(S-PER) Series

The poly(S-PER) series was synthesized following the procedure described by Upton et al.,[13] with some modifications in the mixing process. Briefly, a blend of elemental sulfur (0.1–9.9 g) and PER (0.1–9.9 g) was prepared in 14 mL glass vials, vortexed for 30 s, and sonicated for 15 min to ensure homogenization. The mixture was then magnetically stirred at 1000 rpm and while being heated to 160 °C until it turned a dark red color, before being transferred to a silicon mold for curing at 140 °C in an oven for an additional 18 h. The polymer's nomenclature was generated according to the content of sulfur used [poly(S_a-PER)], where "a" indicates the amount of sulfur (%). For example, the polymer synthesized with 1% sulfur was named poly(S_1-PER).

2.3. Fabrication of Superhydrophobic Films

Liquid coating formulations comprising chloroform, poly(S-PER), and hydrophobic-SiO_2 nanoparticles were prepared as described by Upton et al.[13] These mixtures were sonicated and deposited onto Parafilm M films by spray coating using a compression pump and airbrush gun (Voilamart) at a pressure of 2 bar, as previously reported in the scientific literature[13] (**Figure 1A**). The airbrush spray head was kept ≈4 cm from the substrate during the spraying procedure, with 0.1 mL per cm^2 of the formulations used to ensure even coverage. After spray coating, the films were dried at 50 °C for 2 h to ensure full solvent removal. This process

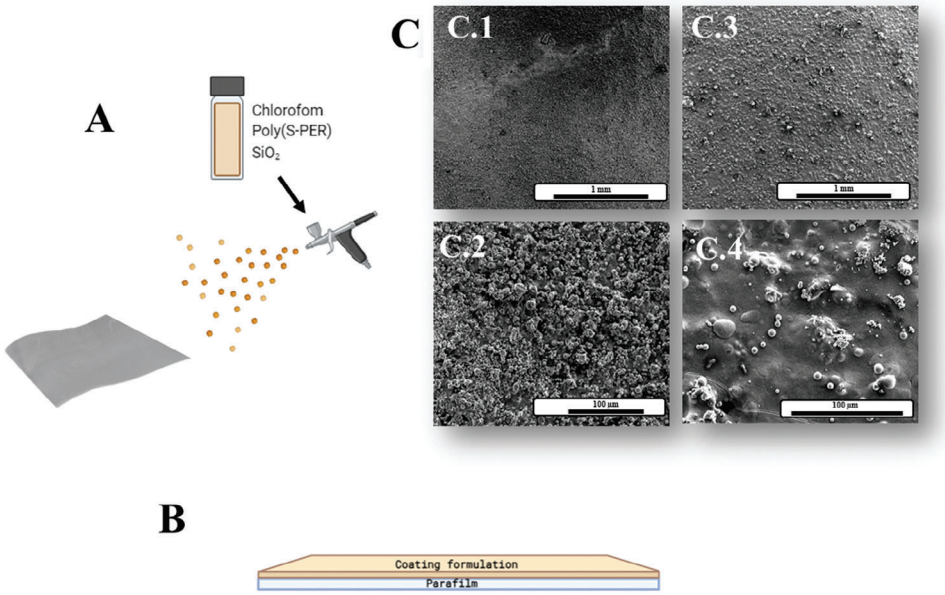

Figure 1. A) Schematic of coating on a substrate; B) two-layer structure of the material; C) Top-down SEM micrographs showing the morphology of (C.1–C.2) $SiO_{2,50}$@poly(S_{50}-PER)$_{70}$ and (C.3–B.4) $SiO_{2,50}$@poly(S_{50}-PER)$_{150}$.

created a two-layer coating with Parafilm M as the bottom layer and sulfur polymer mixed with SiO_2 nanoparticles as the top layer (Figure 1B), which yielded films given the following nomenclature: $SiO_{2,x}$@poly(S_a-PER)$_y$, where a, x, and y are the content of sulfur, the concentration (mg/mL) of SiO_2 and poly(S-PER) in the coating formulation, respectively.

2.4. Characterization

2.4.1. Characterization of Poly(S-PER) Series

Fourier Transform Infrared (FTIR) spectra were recorded using a Bruker Tensor 27 instrument over the wavenumber range of 500 to 4000 cm^{-1}. Nuclear Magnetic Resonance (^{1}H-NMR) analysis utilized a Bruker Advance DRX (400 MHz) spectrometer, with deuterated chloroform as the solvent and tetramethylsilane as the internal standard. Differential Scanning Calorimetry (DSC) measurements were carried out using a TA Instruments Discovery Series DSC 25. A heat-cool-heat method was employed, with heating and cooling rates set at 10 °C min^{-1} under a nitrogen atmosphere, spanning from −60 to 130 °C. Powder X-ray diffraction (PXRD) patterns were collected in reflection mode using a Panalytical X'Pert PRO MPD equipped with a high throughput screening XYZ stage, X-ray focusing mirror, and PIXcel detector. Cu Kα radiation (λ = 1.5406 Å) was utilized, and data were collected over a range of 5–70° (step ≈ 0.03°) using loose powder samples on thin Mylar film within aluminum well plates.

2.4.2. Characterization of Films

Scanning Electron Microscopy (SEM) imaging and Energy-Dispersive X-Ray spectroscopy (EDS) were performed using an FEI Inspect F system with an operational acceleration voltage of 10–20 kV. To enhance electrical conductivity within the SEM, samples were sputter-coated with a thin layer (≈ 10 nm) of gold-palladium (80/20, m/m) using an Automatic Sputter Coater. The Ossila Contact Angle V3.0.0.0 software was used to determine water contact angle (WCAs) using 10 µL water droplets (n = 4) before and after the samples were stretched to 200% of their original length. UV stability was evaluated indirectly by monitoring changes in the WCA over a given exposure period. The coatings were positioned 6.8 cm below a Cole-Parmer Handheld UV Lamp (λ ≈ 254 nm) at a power of 6 W. Mechanical properties of the films were assessed by subjecting them to tension tests on an Instron 68TM-10 testing machine (2 kN static load cell) at an extension rate of 3 mm min^{-1}. The thickness of the coatings was determined using a Laser Scan Micrometer LSM-6000 (N = 10). The size of the fragments after stretching the films was determined using SEM images in combination with ImageJ software.

2.5. Statistical Analysis

Since the measured WCAs were normally distributed (Kolmogorov–Smirnov test, $p > 0.05$), a t-test ($p > 0.05$) was used to determine statistically significant differences between unstretched and stretched samples (n = 4). These analyses were performed using Statistica software. The WCAs are presented as mean ± standard deviation (SD).

3. Results and Discussion

3.1. Synthesis and Characterization of Sulfur Polymers

Since their first report, high-sulfur content polymers have been proposed as a greener alternative to conventional polymers for

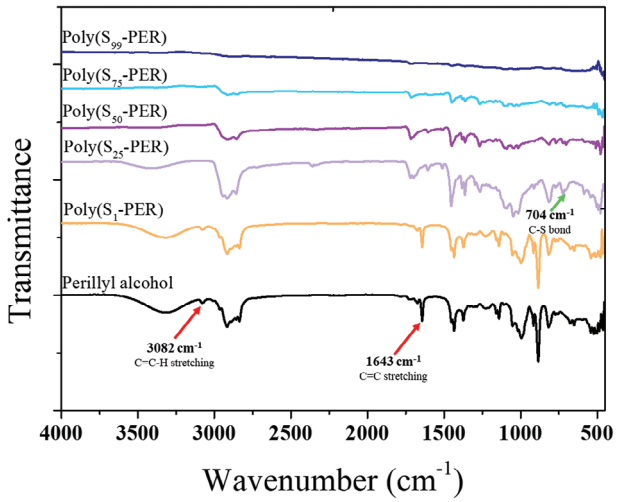

Figure 2. FTIR spectra of perillyl alcohol (PER) and poly(S_a-PER) series, where a indicates the content of sulfur in the polymer.

various applications.[13,23,25,28–31] Due to their versatility, these polymers have been utilized in energy storage,[31] heavy metal adsorption,[29,32] organic pollutant removal,[28,33] antimicrobial materials,[34,35] and superhydrophobic coatings.[13,23,27] Among the crosslinkers that have been used, PER is a monocyclic terpene naturally found in many essential oils,[36] which has been reported before as an interesting alternative to synthesizing high-sulfur content polymers with good solubility in common organic solvents.[13] A series of poly(S-PER) polymers were synthesized with compositions that spanned 1–99 wt.% elemental sulfur to investigate the effects that the crosslinker content had on film wettability.

FTIR spectroscopy was employed to investigate the physical crosslinking within the poly(S-PER) matrix, specifically examining the bonds (i.e., C—S) made between sulfur chains and organic PER molecules. Overall, the FTIR spectra of all poly(S-PER) samples showed a reduction in the intensity of the C≒C—H stretching (3082 cm^{-1}) and C—C stretching (1643 cm^{-1}) signals, while new signals corresponding to C—S bonds (704 cm^{-1}) appeared (**Figure 2**). These results indicate that a reaction took place between the crosslinker and elemental sulfur, as evidenced by the reduction in unsaturated hydrocarbons and the formation of C—S bonds. Notably, the FTIR spectrum of poly(S_1-PER) still exhibited both 3082 and 1643 cm^{-1} signals, indicating the presence of unreacted PER in the polymer. ^{1}H NMR spectroscopy was used to compare the alkene (vinylic and allylic protons) units present in the unreacted PER and the poly(S-PER) series (Figures S1 and S2, Supporting Information). The disappearance of peaks associated with vinylic and allylic protons suggests the consumption of alkene units in the crosslinker, while broad peaks (δ = 1.0–2.5 ppm) typical of polymeric materials and peaks (δ = 3.5–4.0 ppm) suggesting H—C—S bonds appeared in the poly(S-PER) series.[13] Consistent with the FTIR data, unreacted vinylic and allylic protons were observed in the ^{1}H NMR spectrum of poly(S_1-PER).

To investigate the homogeneity of the polymerization, DSC (Figure S3, Supporting Information) and PXRD (Figure S4, Supporting Information) were employed, as these techniques are capable of detecting unreacted elemental sulfur. The DSC curves indicated the presence of crystalline sulfur (105–115 °C) in both poly(S_{75}-PER) and poly(S_{99}-PER), corroborating previous reports that inverse vulcanized polymers synthesized with PER were only stable with sulfur loadings up to 70 wt.%.[13,24] Glass transition temperatures (T_g) calculated from the curves showed that for fully reacted polymers (poly(S_{25}-PER) and poly(S_{50}-PER)), T_g increased with higher elemental sulfur content (T_g for poly(S_{25}-PER) = −2.6 °C, poly(S_{50}-PER) = 28.1 °C). Conversely, T_g decreased as the percentage of unreacted sulfur increased in the final polymer. For instance, the T_g of poly(S_{75}-PER) was 3.2 °C, while for poly(S_{99}-PER), it was −36.9 °C, that a higher weight percentage of sulfur resulted in decreased resistance to physical change and a lower degree of branching or crosslinking when there is unreacted sulfur in the polymer. PXRD data corroborate the DSC findings, showing signs of crystallinity in both poly(S_{75}-PER) and poly(S_{99}-PER), while an amorphous structure was observed in the other polymers in the series. Notably, poly(S_1-PER) was not analyzed by PXRD because it was liquid (viscous) at room temperature. According to Upton et al.,[13] chloroform is the most successful solvent to solubilize the poly(S-PER) series and, therefore, was initially selected for fabricating the superhydrophobic films.

3.2. Fabrication and Characterization of Sulfur-PER-SiO_2 Superhydrophobic Stretchable Films

The initial wettability of each poly(S-PER) was determined by dissolving the polymers into chloroform (70 mg mL^{-1}) and spraying them onto parafilm. A slight trend was observed: an increase in sulfur content correlated with enhanced hydrophobicity (Figure S5, Supporting Information), corroborating previous scientific literature.[13] Additionally, polymers with high-PER content showed slight hydrophilicity, likely due to terminal hydroxyl groups in the PER chemical structure. Poly(S_{99}-PER) exhibited the highest WCA of 141.6° ± 5.2°, which was significantly enhanced by the low solubility of the polymer in chloroform, creating a rough surface. Therefore, Poly(S_{50}-PER) was selected for further characterization/optimization studies.

Most of the polymers initially showed no trapping of air at the surface (a clear Wenzel wetting state).[13] However, by introducing more surface roughness through using SiO_2 nanoparticles, it was possible to achieve superhydrophobicity and a Cassie–Baxter wetting state. Parafilm is composed of a combination of hydrophobic waxes and polyolefins, which gives this stretchable substrate an intrinsic hydrophobic property (WCA of 101.5° ± 5.0°), making it an ideal substrate for fabricating superhydrophobic materials (see Figure S6, Supporting Information for SEM micrographs of uncoated parafilm). The ratio of polymer-nanoparticles is key in generating coherent superhydrophobic coatings.[14,37] Lower loading of SiO_2 nanoparticles can result in flattened surfaces with excess polymer.[13] In comparison, higher loading can create poor quality (non-uniform) and powdery coatings, leading to water penetration and a reduced WCA. Although these coatings may have a higher roughness, they form less effective water-repellent areas and overall increased surface energy due to particle agglomeration, making it favorable for water to spread, thus decreasing the WCA.[38] Therefore, finding an

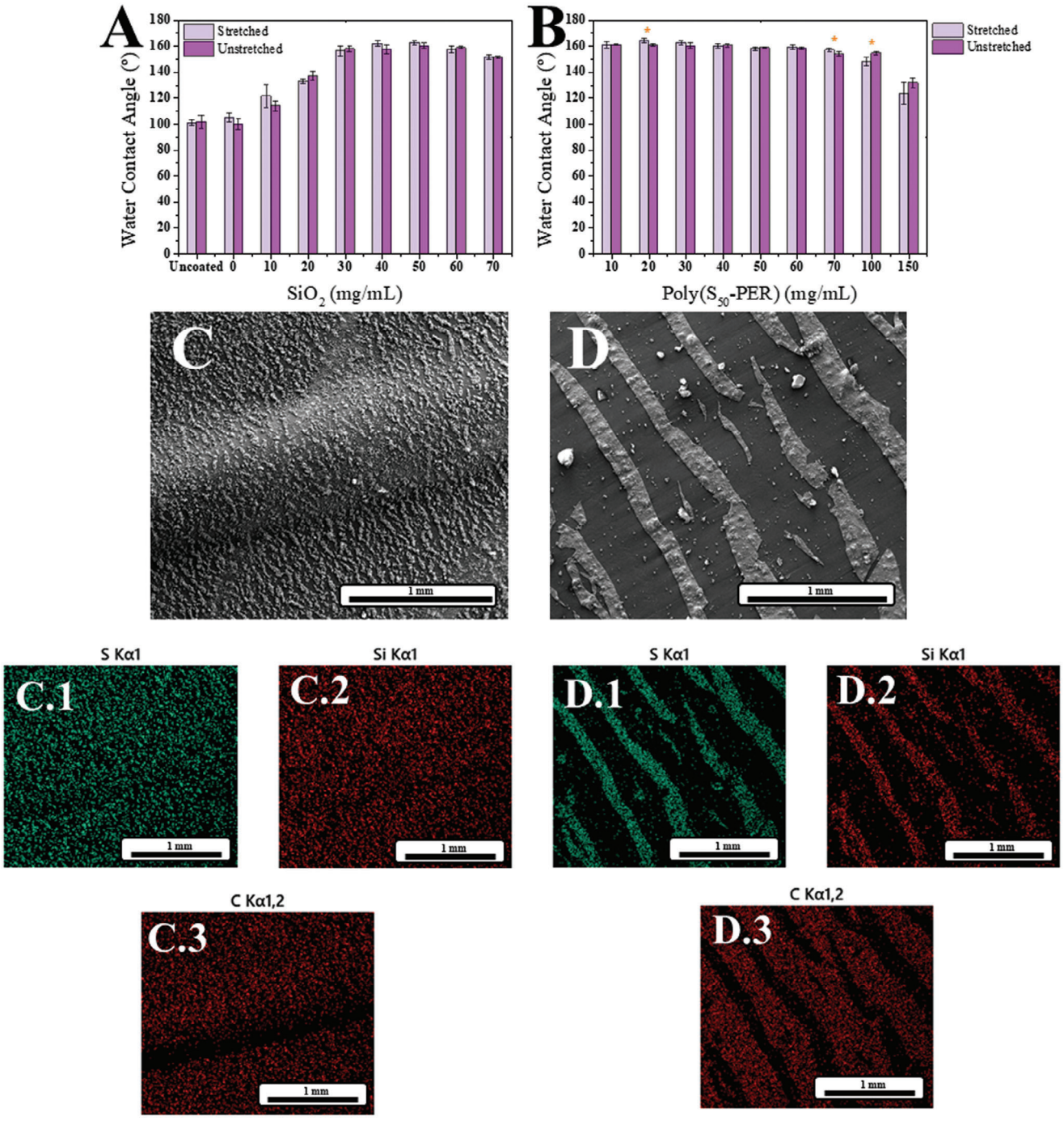

Figure 3. The effect of the A) loading of SiO_2 nanoparticles and B) poly(S50-PER) concentration in the water contact angle in the unstretched and stretched films. *t*-test ($p > 0.05$) was used to determine statistically significant differences between unstretched and stretched samples ($n = 4$). Top-down SEM micrographs showing the morphology of C) $SiO_{2,50}$@poly$(S_{50}$-PER$)_{70}$ and EDS map of sulfur (C.1), silica (C.2), and carbon (C.3), and D) $SiO_{2,50}$@poly$(S_{50}$-PER$)_{150}$ and EDS map of sulfur (D.1), silica (D.2), and carbon (D.3) after stretching.

optimal loading of SiO_2 nanoparticles is crucial for maintaining a high WCA and achieving the desired superhydrophobic properties. To optimize the spray formulation parameters, various loadings of SiO_2 (0–70 mg mL^{-1}) were tested (**Figure 3**). An increase in the WCA was observed with increased loading of SiO_2 nanoparticles, reaching a WCA of 160.0° ± 2.1° at 50 mg mL^{-1}. Additionally, it is worth noting that stretching the films by 200% did not have a statistically significant effect ($p > 0.05$) on the WCA.

An excess of polymer on the surface can lead to a decrease in the WCA. This is principally caused by the generation of a smoother surface texture, diminishing the surface roughness

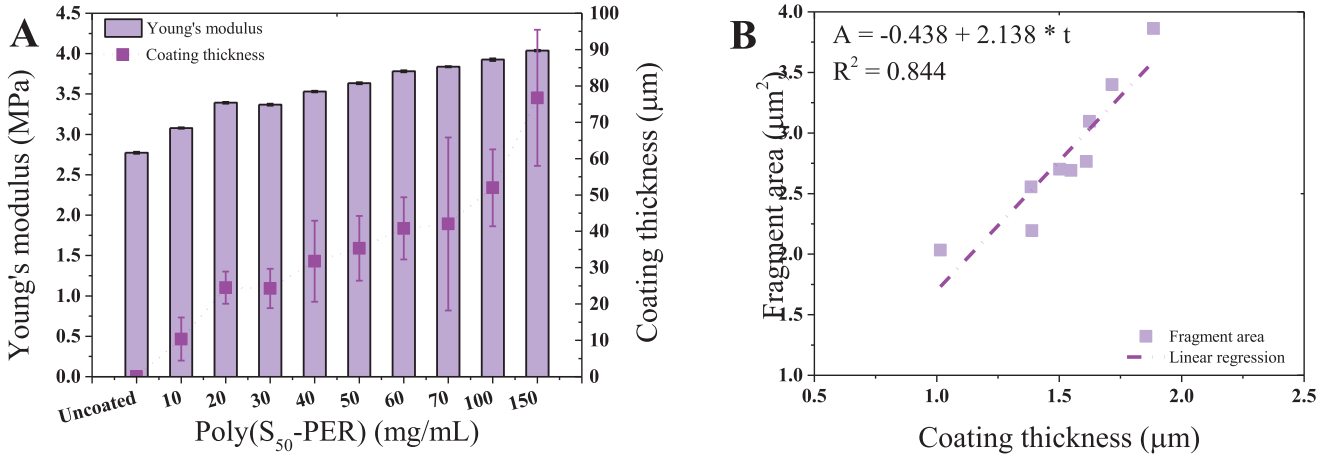

Figure 4. Coating thickness (n = 10) and Young's modulus of the stretchable films. B) Log-log plot of fragment area (post-stretching) versus coating thickness.

necessary for achieving superhydrophobicity.[39] Additionally, certain polymers may contain hydrophilic functional groups (as shown later in this paper) that increase the surface energy, promoting the wetting of water.[13] Consequently, akin to the criticality of determining the optimal loading of SiO_2 nanoparticles, identifying the optimal polymer concentration for incorporation into the spray formulation is imperative to ensure the desired superhydrophobic properties are achieved. For that, various poly(S_{50}-PER) concentrations (0–150 mg.mL^{-1}) were tested. Notably, a concentration of 150 mg mL^{-1} resulted in a decreased WCA. Figure 1 illustrates that at 150 mg mL^{-1}, an excess of polymer is observed on the surface of the coatings, contributing to the observed reduction in WCA. Additionally, it is important to note that poly(S-PER) contains terminal hydroxyl groups, which, in excess, have the potential to diminish the superhydrophobicity of the coatings. Furthermore, the coatings are visually opaque due to the translucent nature of the Parafilm substrate, combined with the yellow-to-orange hue of the polymer solution and the incorporation of SiO_2 nanoparticles, resulting in a non-transparent surface (Figure S7, Supporting Information).

Interestingly, contrary to the observations with varying loadings of SiO_2 nanoparticles, higher polymer concentrations (>70 mg mL^{-1}) led to a decrease in the WCA when the film was stretched. From a concentration of 100 mg mL^{-1} of polymers, a trend of reduction in the WCA was observed, which was particularly evident at 150 mg mL^{-1}. After stretching, the polymer@SiO_2 layer of the film fabricated with a higher polymer concentration broke apart into strips compared to one containing less polymer (Figure 3). EDS mapping revealed that in films fabricated with 70 mg mL^{-1}, even after stretching, the polymer@SiO_2 layer remained uniformly distributed onto the surface of the parafilm (see Figure S7, Supporting Information for a digital image of a water droplet resting on the surface of the coatings. However, in the film fabricated with 150 mg mL^{-1}, larger fragments were formed, resulting in the appearance of uncoated parafilm, which was confirmed by the elemental map of carbon. The emergence of the parafilm, with a lower WCA than the polymer@SiO_2 layer, led to a reduction in the WCA of the entire material. Additionally, FTIR spectra of the films before and after stretching showed more intense characteristic parafilm bands in the films fabricated with 150 mg mL^{-1} after stretching (Figure S8, Supporting Information), corroborating the SEM/EDS data. Since higher concentrations are expected to result in thicker coatings, further investigations were conducted to examine how the thickness of the polymer layer influences the size of the fragments and, consequently, the superhydrophobicity of the films.

3.3. Effect of Coating Thickness on the Top Layer Fragmentation

It was observed that the concentration of polymer in the coating formulation had a distinct impact on the coating thickness. Specifically, higher polymer concentrations resulted in thicker coatings (**Figure 4**). For example, a coating formulation with a concentration of 10 mg mL^{-1} produced coatings with a thickness of 10.34 μm. In contrast, increasing the concentration to 150 mg mL^{-1} led to significantly thicker coatings, measuring 76.73 μm. This clear relationship indicates that as the concentration of polymer in the formulation increases, the resulting coating becomes progressively thicker, reflecting the increased volume of polymer applied.

By analyzing the stress-strain curves (Figure S9, Supporting Information), it was also observed that as the coating thickness increased, the Young's modulus of the films also increased (Figure 4). This trend reflects a clear correlation between coating thickness and Young's modulus values. The data indicates that the polymer layer, which constitutes the top coating, exhibits a higher Young's modulus compared to the underlying parafilm. This was further confirmed by Equation (1), which calculated the Young's modulus of the polymer to be 7.0 MPa, in contrast to the 2.8 MPa measured for the uncoated parafilm. This finding highlights that thicker coatings not only alter the physical dimensions of the films but also modify their mechanical properties, resulting in increased rigidity and structural integrity.

$$Y_{film} = Y_{parafilm} * \frac{thickeness_{parafilm}}{thickness_{film}} + Y_{polymer} * \frac{thickeness_{polymer}}{thickness_{film}} \quad (1)$$

Table 1. Polymer concentration, thickness of the top layer, and fragment area after stretching the films.

Polymer concentration [mg mL^{-1}]	Thickness of top layer [μm][b)]	Fragment area [μm^2][c)]
Uncoated parafilm	13.9 ± 2.3[a)]	Uncoated
10	10.3 ± 3.4	108.1 ± 114.1
20	24.5 ± 7.7	156.2 ± 222.6
30	24.3 ± 8.7	358.2 ± 518.6
40	31.8 ± 10.9	501.5 ± 786.4
50	35.3 ± 15.0	490.4 ± 666.1
60	40.8 ± 10.7	581.8 ± 1216.5
70	42.0 ± 31.2	1250.1 ± 2110.6
100	52.0 ± 18.4	2505.9 ± 3888.2
150	76.3 ± 24.1	7284.3 ± 10 258.1

[a)] Thickness of uncoated parafilm; [b)] Thickness of the film minus thickness of uncoated parafilm; [c)] Estimated using ImageJ, as presented in Figure S10 (Supporting Information). The standard deviation for thickness $n = 10$ and fragment area is automatically estimated by ImageJ.

where, Y_{film}, $Y_{parafilm}$, $Y_{polymer}$ are the Young's modulus of the superhydrophobic film, parafilm, and polymer, respectively. $thickness_{film}$, $thickeness_{parafilm}$, $thickeness_{polymer}$ are the thickness of the superhydrophobic film, parafilm, and polymer, respectively.

As indicated in this study, the thickness of the top layer coating is crucial for maintaining the superhydrophobic properties of the films after stretching. A critical threshold was identified at a polymer concentration of 70 mg mL^{-1}, which corresponds to a coating thickness of 42 μm (**Table 1**). Coatings with polymer concentrations above this threshold showed degradation in their superhydrophobic properties after stretching, while those below this concentration did not experience such impairment (Figure 3). As shown in Table 1, the increased thickness of the top layer results in larger fragments after stretching, leading to the formation of uncoated parafilm islands (Figure 3). These islands have reduced roughness compared to the polymer@SiO_2 fragments, which diminishes the wettability of the films.

Further understanding of how the fragment area is affected by the thickness of the polymer layer requires a deeper comprehension of how thin films fragment on substrates (See Text S1, Supporting Information). Briefly, consider an atomic layer on a substrate under strain. As the strain increases, the thin layer fragments at a critical point. With further strain, fragmentation becomes finer until the thin film starts sliding over the substrate. At this point, fragments separate, releasing stored elastic energy and initiating the first level of fragmentation. Advanced fracture theories suggest that fragmentation or sliding occurs when both the energy release rate and maximum stress reach critical values simultaneously.[40–42]

The energy balance during crack propagation requires that the change in total potential energy equals the work needed to create new fracture surfaces, considering the fracture energy per unit area. Assuming linearity for the constitutive law of the film, Clapeyron's theorem applies (i.e., the variation of the elastic strain energy is equal to half the variation of the external work), which allows correlation of the strain conditions, film surface area, thickness, Young's modulus, and fracture conditions (fracture energy and work required for creating a new surface of fragments). Therefore, the correlation between coating thickness and fragment area at a maximum strain is expected to follow a power law of 1 (Equation 2). When extrapolated to a 2D system, this becomes 2 (i.e., the slope of the linear regression on a log-log scale, as expressed in Equation 3). In our experiments, this slope was calculated as 2.138 (Figure 4), confirming the validity of the model and that coating thickness and fragment area are intrinsically correlated. It is noteworthy that fragmentation is also expected to be strain-dependent (see Text S1, Supporting Information); however, this should be confirmed in future studies.

$$W = kt^a \tag{2}$$

$$\log(W) = \log(k) + a * \log(t) \tag{3}$$

where W is the characteristic fragment size/square root of the fragment area, t is the thickness (μm), a is the exponent, predicted to be 1 from the fragmentation model (see S1, Supporting Information), and k is a constant, predicted to be the ratio between fracture and adhesion energies from the fragmentation model (see S1, Supporting Information); thus a power law scaling between fragmentation area and thickness with the exponent ≈2 is predicted, as experimentally observed (Figure 4B).

3.4. Solvent Investigation and UV Stability

Previous studies have identified chloroform as the ideal solvent for spraying inverse vulcanization sulfur polymers onto substrates; however, its health risks are well-documented.[43] Consequently, alternative solvents were tested to replace chloroform. Among the solvents tested, petroleum ether, hexane, isopropanol, and acetone showed a lack of solubility for poly(S_{50}-PER) (Figure S11, Supporting Information). Conversely, poly(S_{50}-PER) exhibited suitable solubility (70 mg mL^{-1}) in dimethylformamide, tetrahydrofuran, 2-methyltetrahydrofuran, and toluene. After spraying these formulations onto parafilm, the resulting WCAs were similar to those achieved with chloroform (Figure S12, Supporting Information). Despite this, some of these solvents, such as dimethylformamide, tetrahydrofuran, and toluene, are also known to be hazardous, necessitating their replacement with less harmful alternatives.[44] Therefore, 2-methyltetrahydrofuran, a bio-based solvent derived from lignocellulosic biomass such as corncobs and sugarcane bagasse, emerges as a promising alternative for spray-coating applications.[45] Although the coatings maintained their properties after common physical handling or touching, mechanical robustness tests could not be successfully performed due to the fragility of the Parafilm substrate, which consistently tore during each attempt.

Inverse vulcanization sulfur polymers, such as poly(S-PER), are also known for their photocatalytic activity, which can lead to beneficial self-cleaning properties but also degradation of the polymer and S—S bonds.[13,28] To evaluate the UV stability of these materials, films fabricated with chloroform and 2-methyltetrahydrofuran were exposed to UV-C (λ = 254 nm, 6 W), with the WCA measured every 30 min. It was observed that the WCA started to decrease after 150 min of irradiation

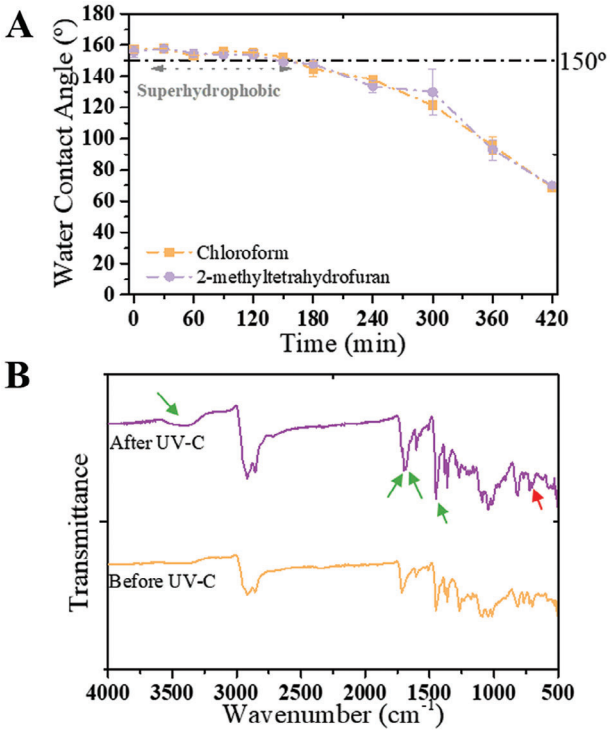

Figure 5. A) Variation in water contact angle with UV-C irradiation. B) FTIR spectra of poly(S_{50}-PER) before and after UV-C irradiation.

for both formulations, resulting in WCAs of 68.8° ± 1.6° and 69.9° ± 0.7° after 420 min of irradiation for chloroform and 2-methyltetrahydrofuran, respectively (**Figure 5**). The decrease in WCA was likely due to the oxidation of poly(S_{50}-PER), as confirmed by FTIR analysis, which showed new O—H and C≐O bands (≈ 3400 and 1680 – 1700 cm^{-1}) and intensified S≐O bands (≈ 1400 cm^{-1}) (Figure 5). Additionally, the breakdown of poly(S_{50}-PER) was indicated by the reduction of C—S bonds (704 cm^{-1}). Despite their limited UV stability, the stretchable films produced here demonstrated 1.7-fold longer UV stability compared to those reported in the literature with the same polymer,[13] while highlighting a facile and environmentally friendly method to produce stretchable superhydrophobic films. Future research should explore the use of alternative cross-linking agents to further enhance the UV stability of inverse vulcanization polymers and, consequently, stretchable films.

4. Conclusion

In this study, we successfully developed stretchable superhydrophobic films by coating parafilm with inverse vulcanization sulfur polymers and incorporating SiO_2 nanoparticles to achieve a Cassie–Baxter state. The optimal formulation, consisting of 70 mg mL^{-1} of polymer and 50 mg mL^{-1} of SiO_2 nanoparticles with 50% PER polymer, demonstrated robust superhydrophobic properties. We identified a critical coating thickness of 42 µm, beyond which the material's superhydrophobic properties were impaired due to the formation of larger fragments (i.e., island of uncoated parafilm). Further investigation revealed a log-log linear correlation with a slope of 2.138 between thickness and fragment area, validating thin film fragmentation on the substrate mathematical model proposed and highlighting the importance of controlling coating thickness for maintaining superhydrophobicity after stretching.

Furthermore, our research addressed the environmental concerns associated with traditional solvents by demonstrating that 2-methyltetrahydrofuran, a bio-based solvent, is a viable alternative to chloroform without compromising the film's properties. The fabricated films also showed enhanced UV stability compared to other sulfur polymer coatings. This work not only provides a facile, straightforward, and sustainable method for producing stretchable superhydrophobic films but also contributes to the broader understanding of the relationship between coating thickness and fragmentation behavior. Future studies should explore the strain-dependent nature of fragmentation and further optimize the formulation for various practical applications.

Supporting Information

Supporting Information is available from the Wiley Online Library or from the author.

Acknowledgements

The authors are grateful for the scholarships provided by the São Paulo State Research Foundation (FAPESP) to V.D. (#2021/08123-0 and #2022/11350-1). In addition, CRC would like to thank the EPSRC (EP/X525613/1) for its research funding.

Conflict of Interest

The authors declare no conflict of interest.

Author Contributions

V.D. conceptualization, data curation, formal analysis, investigation, methodology, and visualization. N.M.P. conceptualization, formal analysis, investigation, methodology, and visualization. S.R. funding acquisition, supervision, visualization. C.R.C. conceptualization, funding acquisition, methodology, project administration, supervision, visualization. All the authors participated in the writing of the original draft.

Data Availability Statement

The data that support the findings of this study are available from the corresponding author upon reasonable request.

Keywords

elastic, fragmentation, parafilm, sulfur, thin films

Received: November 11, 2024
Revised: December 16, 2024
Published online: January 16, 2025

[1] T. Darmanin, F. Guittard, *Mater. Today.* **2015**, *18*, 273.
[2] C. R. Crick, I. P. Parkin, *Chem.-Eur. J.* **2010**, *16*, 3568.
[3] Y. Lu, S. Sathasivam, J. Song, C. R. Crick, C. J. Carmalt, I. P. Parkin, *Science.* **2015**, *347*, 1132.

[4] V. Diniz, J. C. Bear, S. Rath, C. R. Crick, *Surf. Interfaces.* **2024**, *51*, 104691.
[5] A. B. D. Cassie, S. Baxter, *Trans. Faraday Soc.* **1944**, *40*, 546.
[6] A. B. D. Cassie, *Discuss. Faraday Soc.* **1948**, *3*, 11.
[7] Y. A. Mehanna, E. Sadler, R. L. Upton, A. G. Kempchinsky, Y. Lu, C. R. Crick, *Chem. Soc. Rev.* **2021**, *50*, 6569.
[8] L. S. Zhang, C. R. Crick, R. J. Poole, *Appl. Phys. Lett.* **2023**, *123*, 064101.
[9] T. P. Rasitha, N. G. Krishna, B. Anandkumar, S. C. Vanithakumari, J. Philip, *Adv. Colloid Interface Sci.* **2024**, *324*, 103090.
[10] Y. H. Cai, J. Zhang, B. Yue, J. Wu, Y. Yu, J. Hu, J. Qu, D. Tian, *Prog. Org. Coat.* **2023**, *182*, 107700.
[11] E. Sadler, C. R. Crick, *Sustain. Mater. Techno.* **2021**, *29*, e00321.
[12] S. M. Kang, K. Kim, S. Kim, D. G. Lee, T. An, G. H. Kim, *Adv. Mater. Interfac.* **2024**, *11*, 2300627.
[13] R. L. Upton, R. A. Dop, E. Sadler, A. M. Lunt, D. R. Neill, T. Hasell, C. R. Crick, *J. Mater. Chem. B.* **2022**, *10*, 4153.
[14] R. L. Upton, C. R. Crick, *Mol. Syst. Des. Eng.* **2020**, *5*, 876.
[15] X. Li, S. Du, C. Ma, T. Shi, W. Qi, H. Yang, *Ceram. Int.* **2024**, *50*, 9469.
[16] K. Ellinas, A. Tserepi, E. Gogolides, *Adv. Colloid Interfac.* **2017**, *250*, 132.
[17] W. D. Liu, X. J. Wang, S. Y. Xiang, Y. C. Lian, S. Y. Tao, *Processes.* **2024**, *12*, 124.
[18] P. Wang, W. Wei, Z. Li, W. Duan, H. Han, Q. Xie, *J. Mater. Chem. A.* **2020**, *8*, 3509.
[19] F. A. M. Khairuddin, A. A. Rashid, C. P. Leo, G. K. Lim, A. L. Ahmad, H. M. Lim, I. C. S. Tan, *Prog. Org. Coat.* **2022**, *171*, 107024.
[20] Y. Xue, Z. Wang, A. Dutta, X. Chen, P. Gao, R. Li, J. Yan, G. Niu, Y. Wang, S. Du, H. Cheng, L. Yang, *Chem. Eng. J.* **2023**, *465*, 142774.
[21] D. Son, J. H. Koo, J.-K. Song, J. Kim, M. Lee, H. J. Shim, M. Park, M. Lee, J. H. Kim, D.-H. Kim, *ACS Nano.* **2015**, *9*, 5585.
[22] X. J. Su, H. Q. Li, X. J. Lai, Z. H. Chen, X. R. Zeng, *ACS Appl. Mater. Inter.* **2018**, *10*, 10587.
[23] C. C. Miao, et al., *ACS Appl. Polym. Mater.* **2022**, *4*, 4901.
[24] D. J. Parker, S. Y. Chong, T. Hasell, *RSC Adv.* **2018**, *8*, 30429.
[25] M. J. H. Worthington, R. L. Kucera, J. M. Chalker, *Green Chem.* **2017**, *19*, 2748.
[26] W. J. Chung, J. J. Griebel, E. T. Kim, H. Yoon, A. G. Simmonds, H. J. Ji, P. T. Dirlam, R. S. Glass, J. J. Wie, N. A. Nguyen, B. W. Guralnick, J. Park, Á. Somogyi, P. Theato, M. E. Mackay, Y.-E. Sung, K. Char, J. Pyun, *Nat. Chem.* **2013**, *5*, 518.
[27] C. Miao, P. Yan, H. Liu, S. (.D.). Cai, L. J. Dodd, H. Wang, X. Deng, J. Li, X.-C. Wang, X. Hu, X. Wu, T. Hasell, Z.-J. Quan, *B Chem. Soc. Jpn.* **2022**, *95*, 1253.
[28] V. Diniz, J. C. Bear, S. Rath, C. R. Crick, *Sci. Rep.-Uk.* **2024**, *14*, 8144.
[29] J. C. Bear, J. D. McGettrick, I. P. Parkin, C. W. Dunnill, T. Hasell, *Micropor. Mesopor. Mat.* **2016**, *232*, 189.
[30] J. C. Bear, W. J. Peveler, P. D. McNaughter, I. P. Parkin, P. O'Brien, C. W. Dunnil, *Chem. Commun.* **2015**, *51*, 10467.
[31] A. Alex, N. K. Singha, S. Choudhury, *Curr. Opin. Electroche.* **2023**, *39*, 101271.
[32] R. Amna, S. M. Alhssan, *J. Ind. Eng. Chem.* **2024**, *138*, 365.
[33] H. Berk, M. Kaya, M. Topcuoglu, N. Turketen, Y. Karatas, A. Cihaner, *React. Funct. Polym.* **2023**, *187*, 105581.
[34] R. A. Dop, D. R. Neill, T. Hasell, *ACS Appl. Mater. Inter.* **2023**, *15*, 20822.
[35] R. A. Dop, D. R. Neill, T. Hasell, *Biomacromolecules.* **2021**, *22*, 5223.
[36] T. M. C. Chen, C. O. da Fonseca, D. Levin, A. H. Schoenthal, *Pharmaceutics.* **2021**, *13*, 2167.
[37] R. L. Upton, Z. Davies-Manifold, M. Marcello, K. Arnold, C. R. Crick, *Mol. Syst. Des. Eng.* **2020**, *5*, 477.
[38] X. Zhao, Y. Li, B. Li, T. Hu, Y. Yang, L. Li, J. Zhang, *J. Colloid Interf. Sci.* **2019**, *542*, 8.
[39] Z. S. Hu, X. Y. Zen, J. Gong, Y. L. Deng, *Colloid Surf. A.* **2009**, *351*, 65.
[40] N. M. Pugno, R. S. Ruoff, *Philos. Mag.* **2004**, *84*, 2829.
[41] N. M. Pugno, *Int. J. Fract.* **2006**, *140*, 159.
[42] N. Pugno, *Int. J. Fract.* **2006**, *141*, 313.
[43] D. R. Joshi, N. Adhikari, *J. Pharm. Res. Int.* **2019**, *28*, 1.
[44] F. P. Byrne, S. Jin, G. Paggiola, T. H. M. Perchey, J. H. Clark, T. J. Farmer, A. J. Hunt, C. Robert McElroy, J. Sherwood, *Sustain. Chem. Process.* **2016**, *4*, 7.
[45] R. I. Garcia-Gonzalez, C. R. Crick, *AIP Adv.* **2023**, *13*, 105231.

ADVANCED MATERIALS INTERFACES
Open Access

Supporting Information

for *Adv. Mater. Interfaces*, DOI 10.1002/admi.202400896

The Fabrication of Fluorine-Free Stretchable Superhydrophobic Films Using Inverse Vulcanization Sulfur Polymer

Vinicius Diniz, Nicola M. Pugno, Susanne Rath and Colin R. Crick**

Supplementary information: THE FABRICATION OF FLUORINE-FREEE STRETCHABLE SUPERHYDROPHOBIC FILMS USING INVERSE VULVANIZATION SULFUR POLYMER

Vinicius Diniz[1,2*], Nicola M. Pugno[1,3], Susanne Rath[2] and Colin R. Crick[1*]

[1]School of Engineering and Materials Sciences, Queen Mary University of London, London, E1 4NS, UK.

[2]Institute of Chemistry, University of Campinas, 13083-970 Campinas, Brazil.

[3]Laboratory for Bioinspired, Bionic, Nano, Meta Materials and Mechanics, Department of Civil, Environmental and Mechanical Engineering, University of Trento, via Mesiano 77, Trento, Italy.

*Authors for correspondence: *c.crick@qmul.ac.uk*

---- Perillyl alcohol (PER)

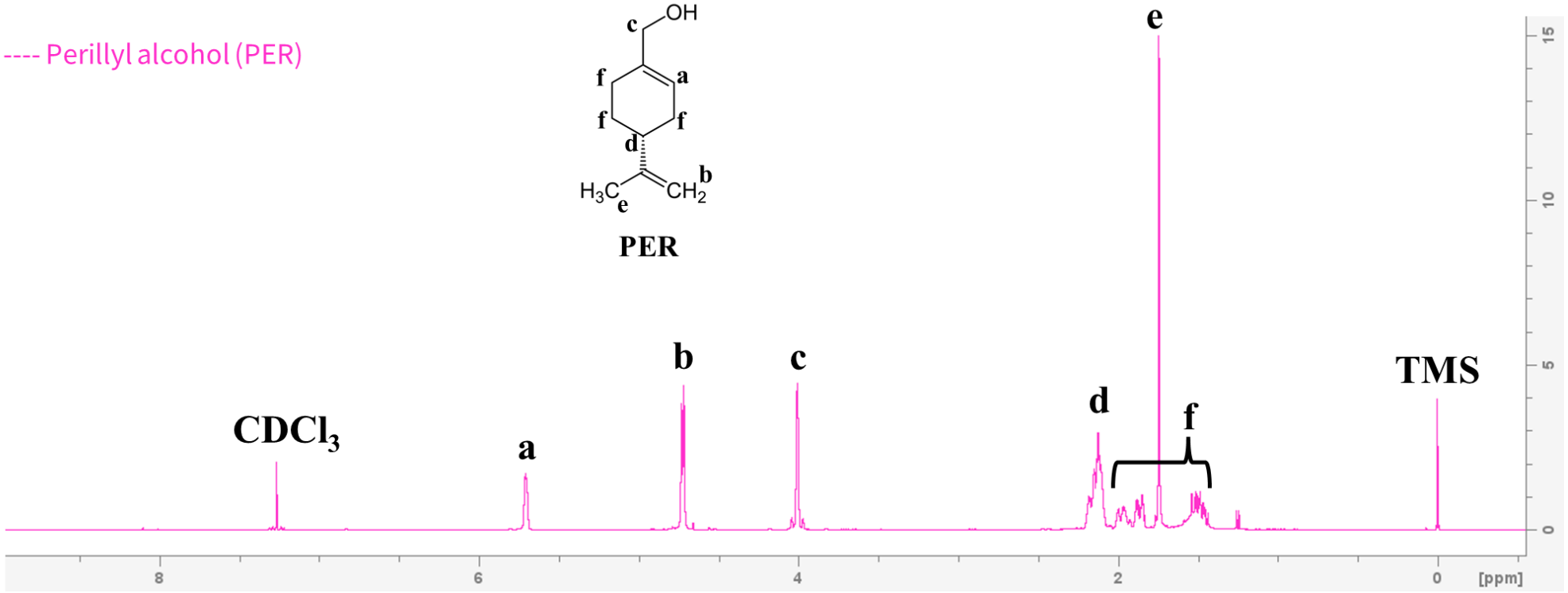

Figure S1: ^{1}H-NMR spectrum of Perillyl alcohol (PER) in $CDCl_3$. TMS: Trimethylsilane

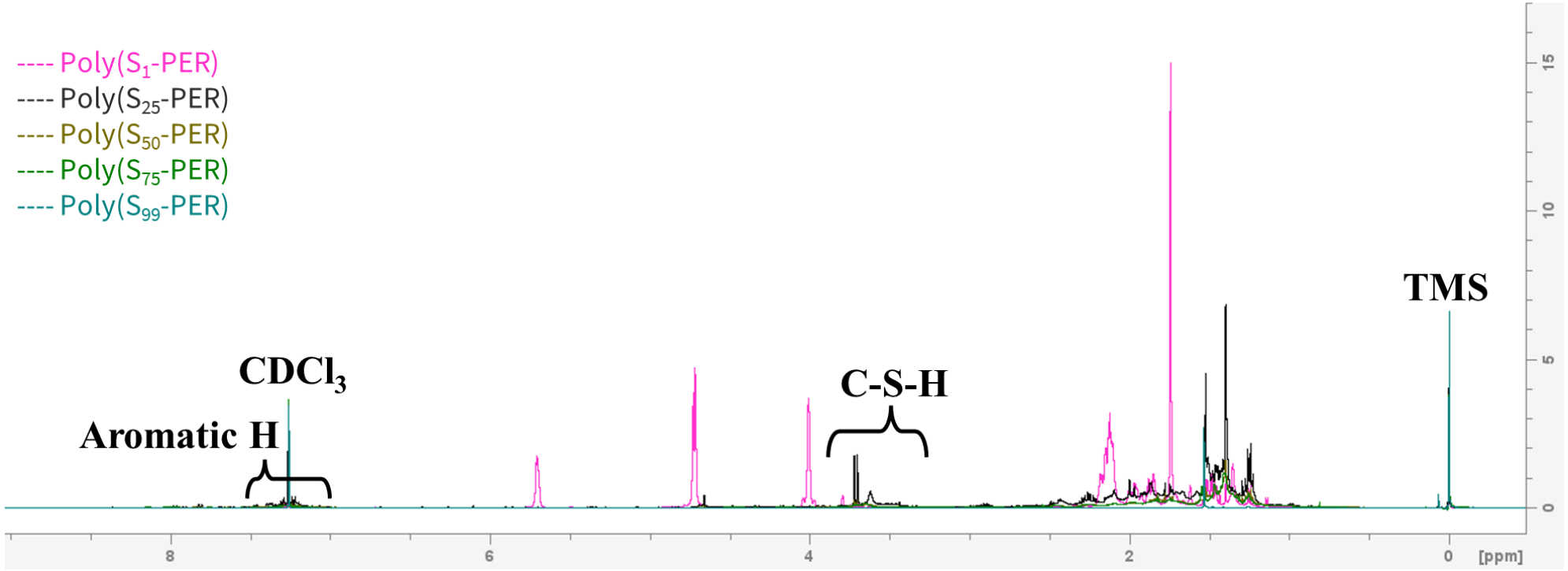

Figure S2: ^{1}H-NMR spectra of poly(S_a-PER) series in $CDCl_3$, where a indicates the content of sulfur (m/m) in the polymer. TMS: Trimethylsilane.

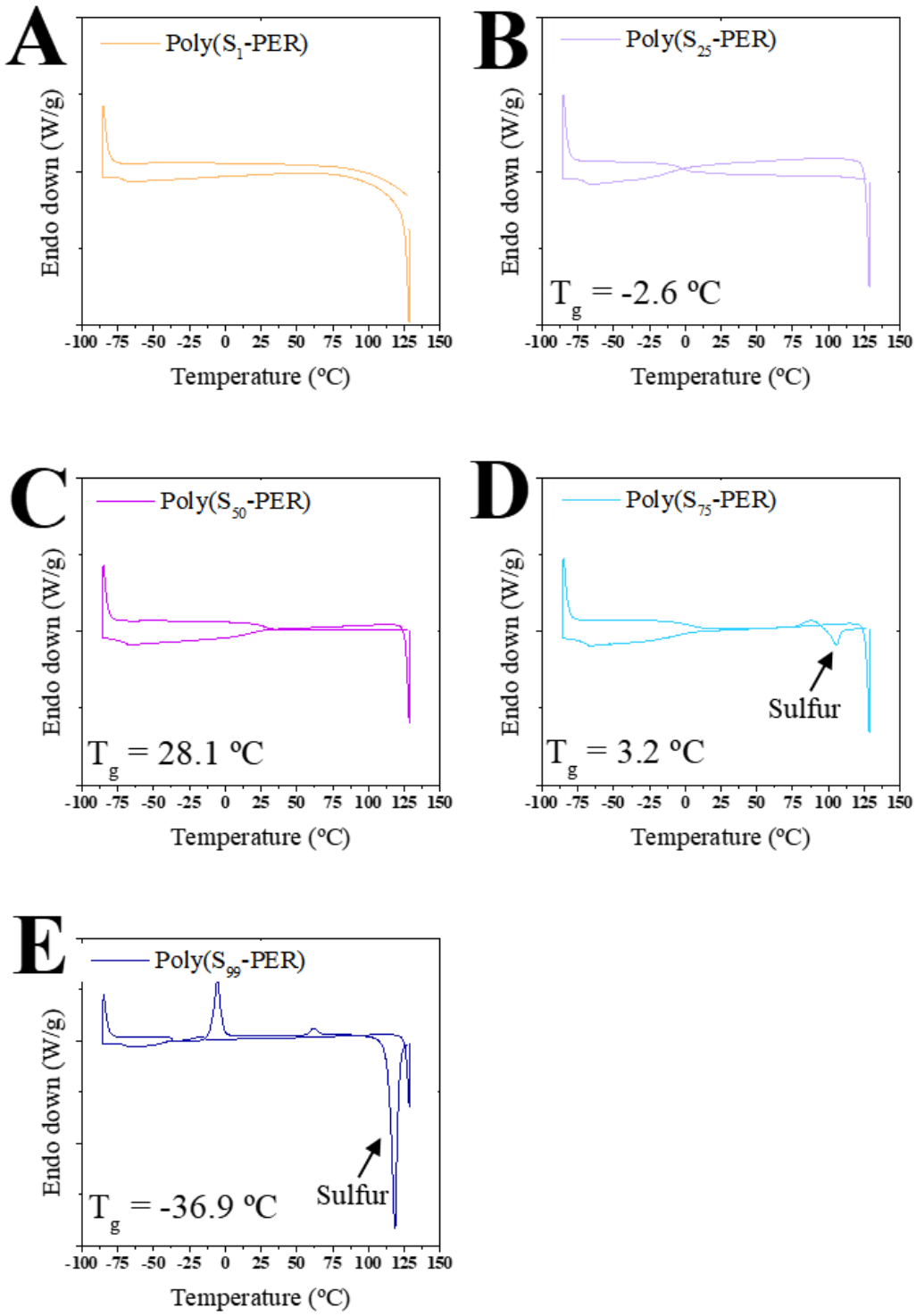

Figure S3: DSC thermogram of poly(S_a-PER) series, where a indicates the content of sulfur (m/m) in the polymer. T_g is the glass transition temperature.

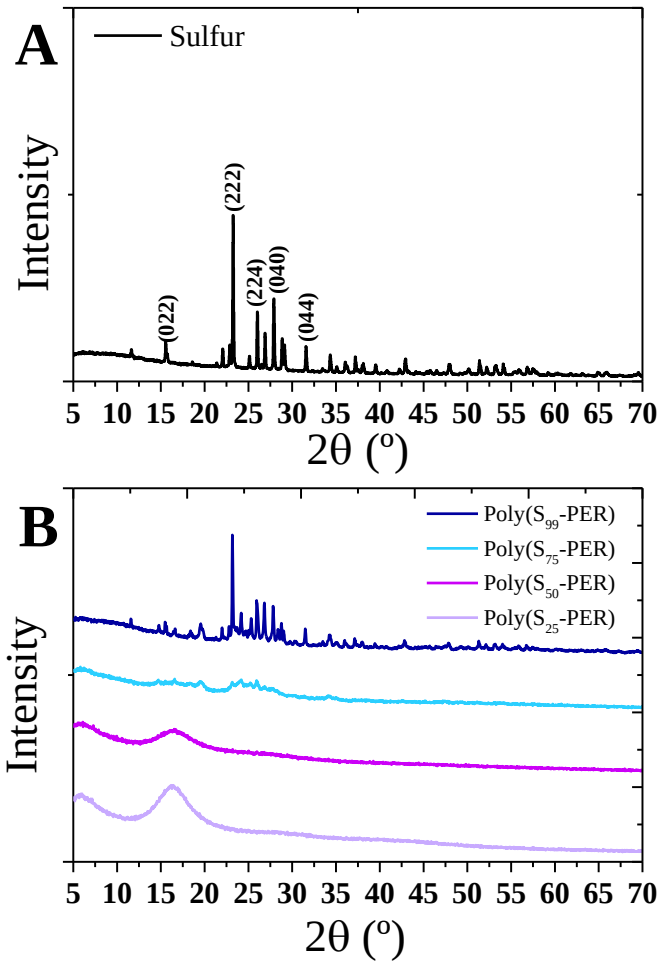

Figure S4: PXRD pattern of elemental sulfur (A) and poly(S_a-PER) series (B), where a indicates the content of sulfur (m/m) in the polymer.

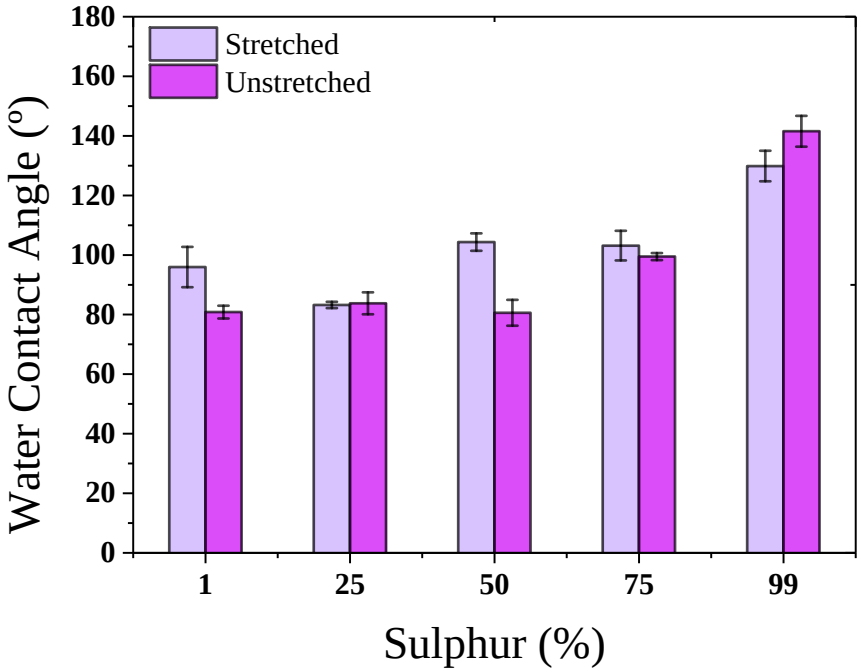

Figure S5: Wettability of poly(S-PER) series without SiO_2 nanoparticles. poly(S-PER) concentration = 70 mg/mL into chloroform.

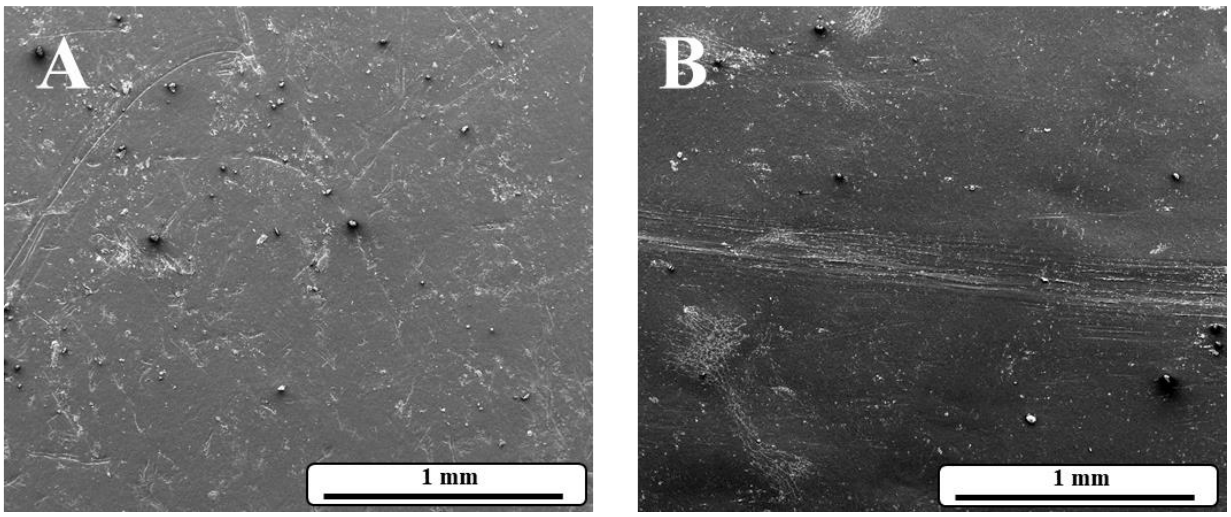

Figure S6: Top-down SEM micrographs showing the morphology of uncoated Parafilm: (A) unstretched and (B) stretched.

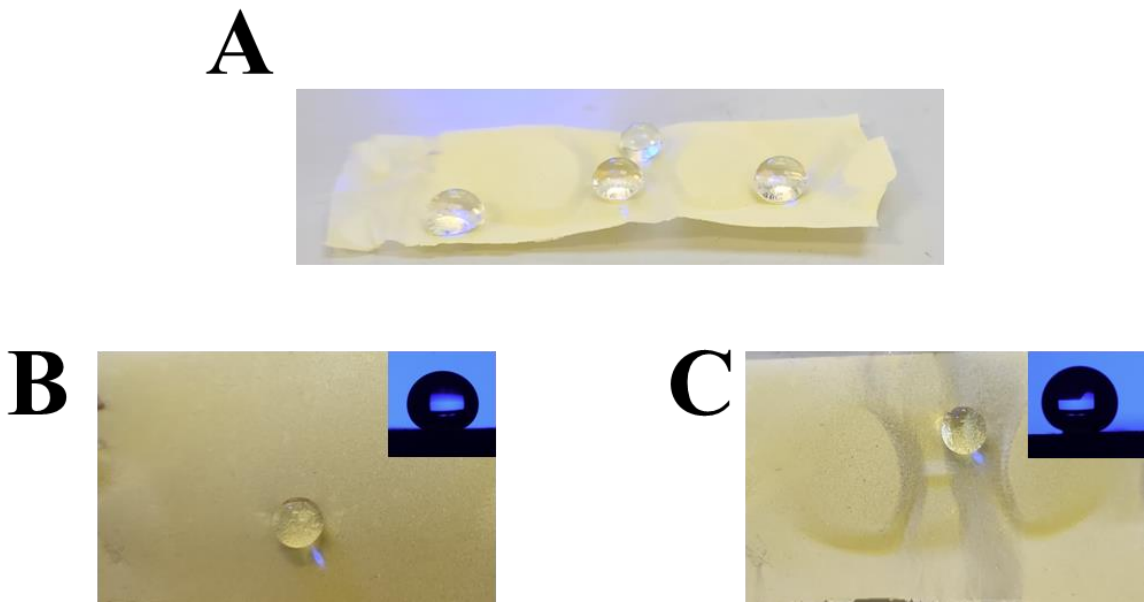

Figure S7: Digital image showing (A) a side view of the poly(S_{50}-PER) coating with both stretched and unstretched sections, (B) a top view of the coating before stretching, and (C) a top view of the coating after stretching.

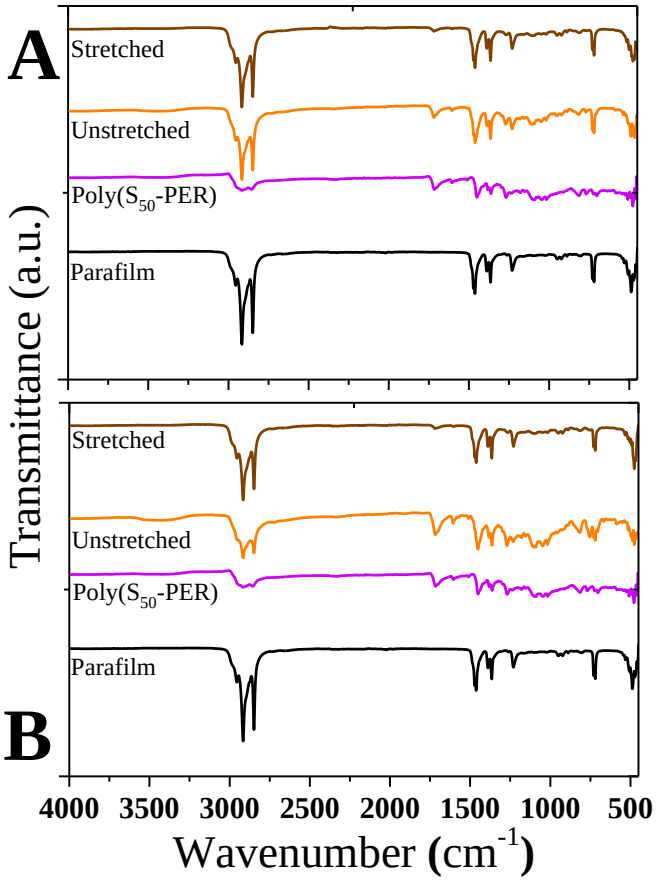

Figure S8: FTIR spectra of the (A) 70 mg/mL film and (B) 150 mg/mL film before and after stretching.

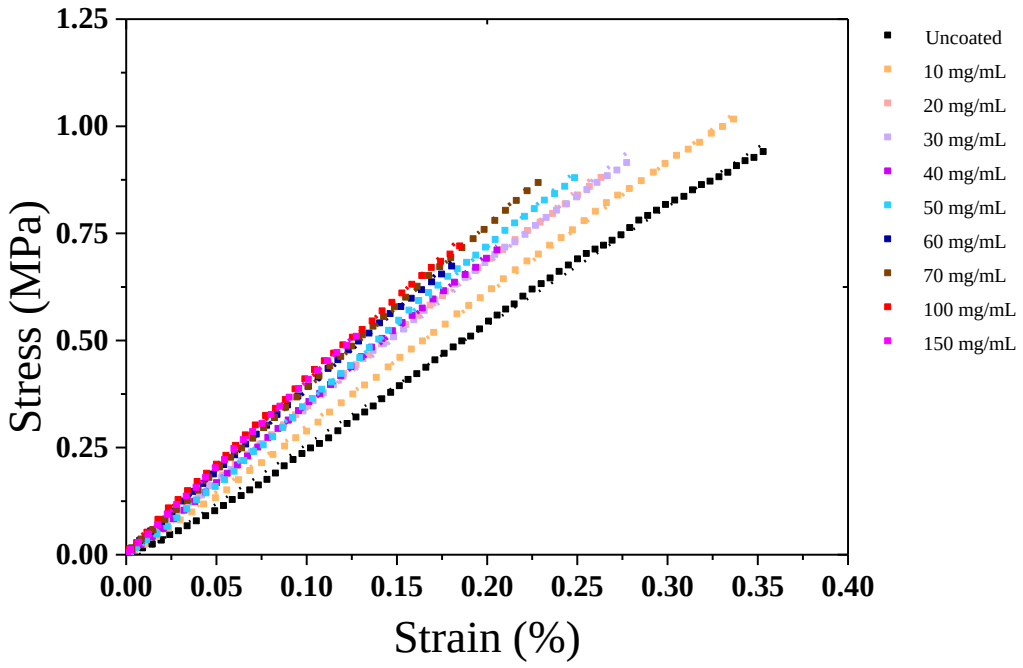

Figure S9: Stress-strain curve of the stretchable films. The uncoated film represents uncoated parafilm.

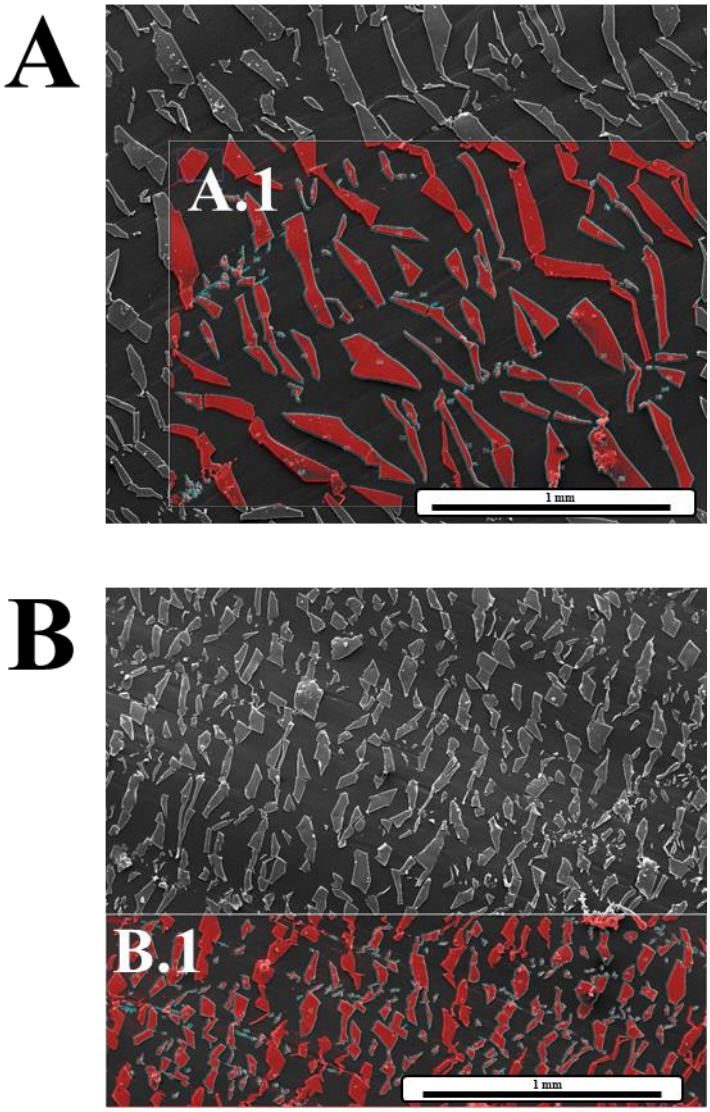

Figure S10: SEM image of (A) 150 mg/mL stretched coating and (A.1) its imageJ reference. SEM image of (B) 100 mg/mL stretched coating and (B.1) its imageJ reference.

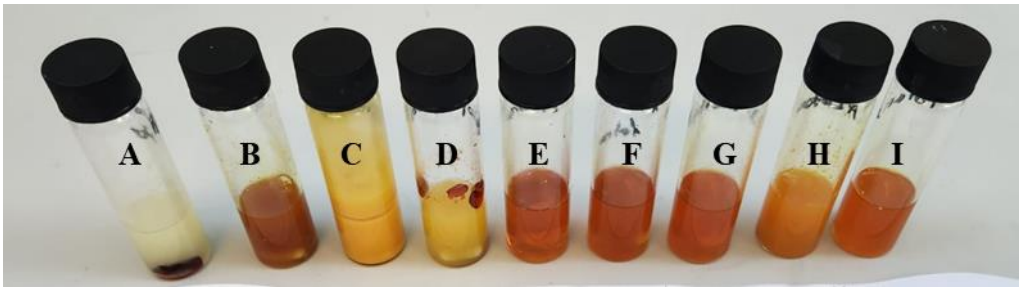

Figure S11: 70 mg/mL of poly(S_{50}-PER) in (A) petroleum ether, (B) dimethylformamide, (C) hexane, (D) isopropanol, (E) chloroform, (F) tetrahydrofuran, (G) 2- methyltetrahydrofuran, (H) acetone, and (I) toluene.

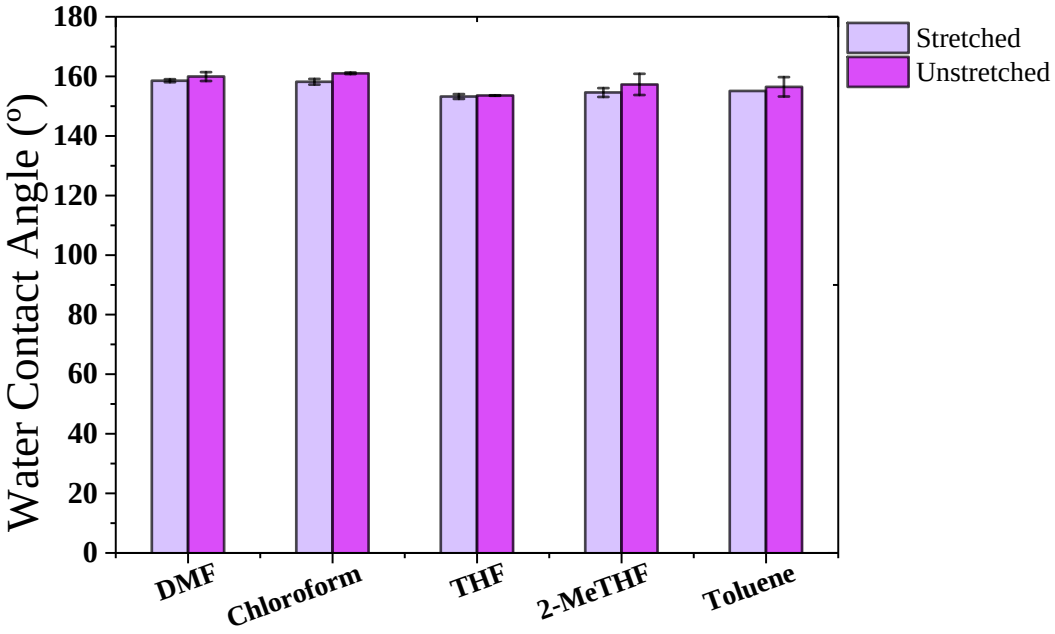

Figure S12: The effect of solvent in the water contact angle (n = 4) in the unstretched and stretched films.

Text S1: Hierarchical fragmentation of thin films on substrates

Consider an atomic layer deposited over a substrate and subjected to strain. At a critical strain, the layer begins to fragment; increasing the strain results in finer fragmentation until the film slides over the substrate. This process releases stored elastic energy and leads to first-level fragmentation. After contraction, the final fragments are similar to the initial film, and fragmentation occurs again, reaching a minimal fragment size related to the material's intrinsic strength. This fragmentation process is depicted in Text S1 Figure 1 (below). This letter aims to predict this complex fragmentation evolution.

According to advanced fracture theories [1-3], fragmentation or sliding occurs when both the energy release rate and the maximum stress reach their critical values simultaneously. These conditions must be coupled to be necessary and sufficient for fragmentation [4].

The energy balance during crack propagation dictates that the change in total potential energy $\mathrm{d}\Pi$, equal to the change in elastic strain energy $\mathrm{d}\Phi$ minus the change in external work $\mathrm{d}\Psi$, must equal the negative of the work spent in creating new surface fragments $\mathrm{d}S$, i.e., $\mathrm{d}\Pi = \mathrm{d}\Phi - \mathrm{d}\Psi = -2\gamma \mathrm{d}S$, where 2γ is the fracture energy per unit area. Assuming linearity in the film's constitutive law validates Clapeyron's theorem, $\mathrm{d}\Phi = \mathrm{d}\Psi/2$. Accordingly, $\mathrm{d}\Pi = -\mathrm{d}\Phi$ and $\mathrm{d}\Phi = 2\gamma \mathrm{d}S$. By integration, we have $\Delta\Phi = 2\gamma\Delta S$, with $\Delta\Phi = \frac{E\left[\varepsilon^{(0)2} - \varepsilon_r^2\right]}{2} At$

Where ε is the applied strain, $A = W_0 L$ is the film surface area, t is its thickness, E is its Young's modulus, $\varepsilon^{(0)} = \varepsilon + \varepsilon_0$ is the strain in the film and ε_0 is the initial pre-strain whereas ε_r is the residual strain after fragmentation. The new crack area created is $\Delta S = Ltn$, where n is the number of strips/fragments. Thus, fragmentation is expected when the following condition (1) holds:

$$\begin{cases} \dfrac{E\left[\varepsilon^{(0)2} - \varepsilon_r^2\right]}{2} At = 2\gamma Ltn \\ \varepsilon^{(0)} = \varepsilon_f \end{cases} \tag{1}$$

Where, ε_f is the material fracture strain;

It is possible to derive the fragment size, or strip width, during stretching as (2):

$$W = \frac{L}{n} = \frac{4\gamma}{E\left[\varepsilon^{(0)2}(W) - \varepsilon_r^2\right]} \tag{2}$$

In (2), the residual stress during fragmentation is unknown and depends on the defect/strength distribution of the layer/fragments. Assuming the validity of Weibull's statistics, a power law consistent with fractal fragmentation [5], we have:

$$\frac{\varepsilon_f}{\varepsilon_c} = \left(\frac{W}{c}\right)^{-\frac{1}{m}} \tag{3a}$$

Where *m* is the Weibull's modulus and *c* is a characteristic width at a reference strain ε_c.
One could consider ε_c as the ideal material strength of the layer and *c* as the minimal fragment width. By comparing the last two equations, the residual strain during fragmentation can be calculated (see Text S1 Figure 1).
Fragmentation begins with excess energy and an initial film strain $\varepsilon_i^{(0)}$, which can be derived from equations (3a) and (1):

$$\frac{\varepsilon_i^{(0)}}{\varepsilon_c} = \left(\frac{W_0}{c}\right)^{-\frac{1}{m}} \tag{3b}$$

The fragmentation state described by equation (3) continues until the film slides over the substrate. Similar to previous analysis, sliding is predicted to occur when the following conditions are met:

$$\begin{cases} \dfrac{E\left[\varepsilon^{(0)2} - \varepsilon_r^2\right]}{2} At = 2\gamma_a A \\ \tau + \tau_0 = \tau_a \end{cases} \tag{4}$$

where γ_a is the adhesion energy, τ is the shear stress, τ_0 is the shear pre-stress and τ_a is the adhesive shear strength.

For the film failure strain, we assume size-dependent adhesion strength based on Weibull's statistics:

$$\frac{\tau_a}{\tau_c} = \left(\frac{W}{c}\right)^{-\frac{1}{q}} \tag{5}$$

where *q* is the Weibull's modulus and τ_c is the ideal adhesion strength at the minimal size scale *c*.

To connect normal and shear stresses, we use the following force equilibrium in the sliding-shear model:

$$\frac{W\left(\tau + \tau_0\right)}{2} = E\varepsilon^{(0)} t \tag{6}$$

By inserting equation (6) into equation (5), we can derive the fragment size at which abrupt sliding occurs as:

$$W_s^{(0)} = 4\frac{\sqrt{\gamma_0 Et}}{\tau_a} \tag{7}$$

Where γ_0 is the adhesion energy at the initial scale level; at a film strain $\varepsilon_s^{(0)}$ (combining equations (5) and (6)), given by:

$$\varepsilon_s^{(0)} = 2\sqrt{\frac{\gamma_0}{Et}} \tag{8}$$

Or at an applied strain:

$$\varepsilon_1 = 2\sqrt{\frac{\gamma_0}{Et}} - \varepsilon_0 \tag{9}$$

During sliding, the fragments contract by a quantity $\Delta W_s^{(0)} = W_s^{(0)} - W_1$ due to the release of the residual strain, reaching a size that can be computed from equation (2) (see Text S1 Figure 1).

$$W_1 = \frac{4\gamma}{E\varepsilon_s^{(0)2}} = \frac{\gamma}{\gamma_0}t \tag{10}$$

At this point, both sliding and fragmentation at hierarchical level *n*=0 are complete. We have independent fragments of size W_1 in the same condition as the initial film of size W_0. If γ_0 is size-independent, fragmentation ceases even if strain increases, as indicated by the previous approach and noting that $W_2 = W_1$ remains constant. However, for film failure strain, we can assume the interface properties are size-dependent, for example, following Weibull's statistics:

$$\frac{\gamma}{\gamma_0} = \left(\frac{W}{W_0}\right)^{-\frac{1}{q}} \tag{11a}$$

where *q* is its Weibull's modulus. Thus at the second hierarchical level, the adhesion strength is:

$$\frac{\gamma_1}{\gamma_0} = \left(\frac{W_1}{W_0}\right)^{-\frac{1}{q}} \tag{11b}$$

In this case, following the previous approach and noting that $\varepsilon^{(1)} = \varepsilon + \varepsilon_0 - \varepsilon_s$ we predict sub-fragments of size:

$$W_2 = \frac{\gamma}{\gamma_1}t \tag{12}$$

at an applied strain:

$$\varepsilon_2 = 2\sqrt{\frac{\gamma_0}{Et}} + 2\sqrt{\frac{\gamma_1}{Et}} - \varepsilon_0 \tag{13}$$

Thus the hierarchical fragmentations are described by:

$$\frac{\gamma_n}{\gamma_0} = \left(\frac{W_n}{W_0}\right)^{-\frac{1}{q}}, \quad W_{n+1} = \frac{\gamma}{\gamma_n} t, \quad \varepsilon_n = 2\sqrt{\frac{1}{Et}} \sum_{l=0}^{n-1} \sqrt{\gamma_l} - \varepsilon_0 \tag{14}$$

The process, summarized in Text S1 Figure 1, is terminated when $W_n \le c$.

$$c = \frac{4\gamma}{E\varepsilon_c^2} \tag{3c}$$

No further fragmentation occurs even with increased strain. In the limiting case, ideal values in equation (3c) predict a minimal fragment size comparable to atomic spacing, aligning with Orowan's and Quantized Fracture Mechanics predictions [1]. If the layer is subjected to a perpendicular strain (or initially to a bi-axial strain state), similar equations apply along the perpendicular direction(s).

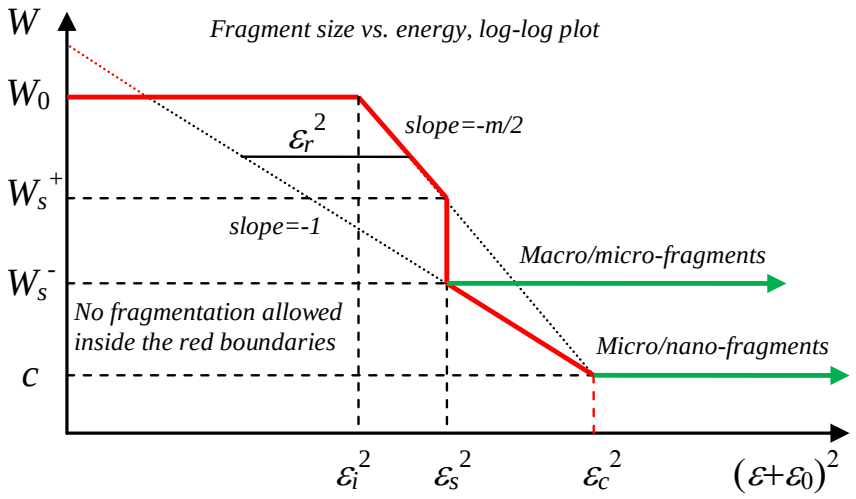

Text S1 Figure 1: Hierarchical and complex fragmentation of thin films on substrates: the red continuous line is followed during fragmentation and fragments approach the green line limits. Note the critical value m=2, and that different relative positions of ε_s in the diagram change qualitatively the shape of the red line and thus the behaviour of the fragmentation. Weibull's equation (slope $-m/2$) could in general be substituted with any other possible state equation and the fragmentation curve (slope -1) can be modified to consider the nonlinear constitutive law of the material.

[1] N. Pugno, R. Ruoff, *Quantized Fracture Mechanics*, PHILOSOPHICAL MAGAZINE (2004), **84/**27, 2829-2845.
[2] N. Pugno, *Dynamic Quantized Fracture Mechanics.* INT. J. OF FRACTURE (2006), **140**, 159-168.
[3] N. Pugno, *New Quantized Failure Criteria: Application to nanotubes and nanowires.* Int. J. OF FRACTURE (2006), **141**, 311-323.
[4] P. Cornetti, N. Pugno, A. Carpinteri, D. Taylor, *Finite Fracture Mechanics: a coupled stress and energy failure criterion*. ENGINEERING FRACTURE MECHANICS (2006), **73**, 2021-2033.
[5] A. Carpinteri, N. Pugno, *One-, two- and three-dimensional universal laws for fragmentation due to impact and explosion,* J. OF APPLIED MECHANICS (2002), **69**, 854-856.